ESTIMATION OF ROTOR MAST MOMENTS USING A DATA-DRIVEN OBSERVER TUNING

Johannes Wartmann, Frederik A. Döring, Susanne Seher-Weiß
German Aerospace Center (DLR), Institute of Flight Systems, Braunschweig, Germany

Abstract

Incorporating main rotor-states like the tip-path-plane flapping angles into the flight control system of a rotorcraft allows for enhanced handling and ride qualities as well as reduced pilot workload. Still, measuring rotor-states in the rotating frame is cost-intensive and more complex than fixed-frame measurements. In this paper, an observer is proposed to estimate the rotor mast bending moments using only fixed-frame measurements. Therefore, linear models of the research rotorcraft ACT/FHS are identified from an extensive flight test campaign. On this basis, different linear observers are designed and optimized using flight data. Two promising observers of different complexity are then selected using a cross-validation. Finally, these observers are analyzed in the time and frequency domain using a variety of different flight maneuvers like sweeps, stable forward flight and flight in turbulence.

NOTATION

ACT/FHS	Active Control Technology / Flying Helicopter Simulator
ci	confidence interval
cv	cross-validation
DLR	Deutsches Zentrum für Luft- und Raumfahrt (German Aerospace Center)
ML	Maximum Likelihood output error method
PBSIDopt	optimized Predictor-Based Subspace Identification (method)
$\boldsymbol{A}, \boldsymbol{B}, \boldsymbol{C}, \boldsymbol{D}$	discrete-time state-space matrices
d_1, $\underline{d}_1$	index of agreement, overall d_1
J_{ave}	average frequency domain cost function
J_{rms}	root mean square error
$\boldsymbol{L}$	observer gain matrix
m_c, m_s	longitudinal and lateral rotor mast moments (in fixed-frame), Nm
n_x, n_u, n_y	number of states, inputs, and outputs
N	number of measurements
p, q, r	roll, pitch and yaw rates, rad/s
T_i	data sets (for $i \in \{\text{train}, \text{test}, 1, \ldots, 10\}$)
u, v, w	aircraft-fixed airspeed components, m/s
$\boldsymbol{u}_k$, $\boldsymbol{x}_k$, $\boldsymbol{y}_k$	discrete-time input, state and output vectors at k-th time step
$\boldsymbol{W}, \boldsymbol{V}$	process and measurement noise covariance matrices (tuning parameters)
$\boldsymbol{y}_{\text{m},k}$	measured output (index m)
$\boldsymbol{y}_{\text{o},k}$	measured outputs used in update step of observer (index o)
$\boldsymbol{z}_k$	performance output vector (rotor mast moments)
β_{1c}, β_{1s}	longitudinal and lateral tip-path-plane flapping angle, rad
δ_x, δ_y	longitudinal and lateral cyclic controls, %
δ_p, δ_0	pedal and collective controls, %
ϕ, θ	roll and pitch attitude angles, rad
ω	angular frequency, 1/s
$\hat{\cdot}$	estimated quantities
$\cdot_{\text{MM}}$	rotor mast moment (used as index)
$\cdot_{\text{RB}}$	rigid body (used as index)

1. INTRODUCTION

Rotorcraft flight control systems benefit from incorporating main rotor-states into the feedback loops [1–3]. It has been shown, that the usage of tip-path-plane flapping angles in addition to the body rates and attitudes in a flight control system leads to improved handling qualities and ride quality as well as reduced pilot workload especially in adverse weather conditions like turbulence and gusts [4, 5]. In detail, rotor-state feedback provides lead to fuselage feedback which can be used to enhance disturbance rejection and stability margins. Flight tests on the RASCAL JUH-60A aircraft showed improved Mission Task Elements performance applying implicit and explicit rotor-state feedback, among others [6].

At the same time, flight controller development aims at carefree maneuvering which requires accounting for

main rotor loads and other structural limits. In [7, 8], the main rotor-states are used to provide tactile cues to avoid the exceedance of the main rotor moments. Furthermore, redundant controls of compound helicopters enable load alleviation in the flight control system without degrading handling qualities [9]. Both rotor-state feedback and load alleviation need accurate rotor-states, i.e. tip-path-plane flapping angles or main rotor moments. Measuring these rotor-states in the rotating frame is still difficult and/or cost-intensive, thus limiting the before-mentioned benefits to large and/or military rotorcraft. Replacing costly sensors by estimation algorithms (i.e. observers) on the other hand would allow rotor-state feedback or rotor load alleviation also for small production rotorcraft.

Different aspects of rotor-state estimation using only measured rigid-body data have been covered in the literature. Two steady-state Kalman filters are designed in [1] to estimate the rotor states from the fuselage pitch and roll angles for a linear roll-pitch-horizontal velocity model of the Sikorsky S-61 rotorcraft. A multiple regression model was applied in [10] to predict main rotor blade bending and pushrod vibratory loads from the control inputs, angular rates, forward velocity and the normal load factor. This work was extended to estimate helicopter component loads in the rotating system to determine fatigue in [11] and [12]. A Kalman filter was designed in [7] to predict and then limit the main rotor hub moments using a force-feel system for a UH-60A GENHEL simulation. A linearized state-space model of the nonlinear simulation was applied as system model. Varying flight conditions are accounted for by using a neural network in [8]. Tip-path-plane flapping angle sensor faults on the RASCAL UH-60 were mitigated by Kalman filter estimates based on a linearized FORECAST model of the UH-60 in [13]. These estimates are subsequently used in a rotor-state feedback flight control system. In [14] rotor loads of the AW609 are predicted by a neural network using measurements from the fixed and rotating frame. Flight test data have only been evaluated in very few of these publications. Apart from neural network predictors, linearized models have been used for an estimator design.

This paper focuses on a data-driven observer design to estimate the rotor mast moments in the fixed rotorcraft frame using rigid-body measurements only. Flight test data of the ACT/FHS (Active Control Technology / Flying Helicopter Simulator) research helicopter are used for this evaluation. The ACT/FHS, its flight test instrumentation including a rotor measurement system as well as the extensive flight test campaign are described in detail. Then, the system identification process of a linear physics-based model and six black-box state-space models is described and evaluated. The identified models of different complexity are compared in detail. Subsequently, the observer design is outlined. The observer structure and the data-driven tuning process are explained. Two promising observers are selected via cross-validation using independent data sets. The chosen observers are analyzed in the time and frequency domain and their ability to replace a rotor measurement system is discussed. The paper finishes with conclusions and an outlook for future work.

2. EXPERIMENTAL SETUP

2.1. The ACT/FHS Research Rotorcraft

The ACT/FHS (Active Control Technology / Flying Helicopter Simulator), as shown in figure 1, is the main aircraft for rotorcraft research at DLR. It is a twin-engine helicopter with fenestron and bearingless main rotor and has a maximum takeoff weight of about 2.9 t.

Figure 1: DLR's research rotorcraft ACT/FHS

The ACT/FHS is based on an Airbus Helicopters H135, but is highly modified. Its mechanical controls are replaced and then upgraded by a full-authority fly-by-wire/fly-by-light control system which allows for experimental flight controls. Thus, the dynamics of the ACT/FHS are not directly comparable to data from a production H135 rotorcraft. The ACT/FHS is equipped with various high fidelity sensors like a noseboom, two differential GPS/SBAS receivers, flight test instrumentation and inertial measurement systems. Furthermore, this sensor suite was completed by a main rotor measurement system in 2018/2019.

Currently, the main rotor measurement system provides, among others, rotor azimuth and main rotor mast bending moments. In figure 2 the sensor signal processor system of the rotor measurement system installed into the rotor head of ACT/FHS is depicted. Data transmissions between the rotating and non-rotating frame is handled by telemetry using HF antennas. Rotor blade flapping signals are currently not measured as the blades have not been instrumented yet.

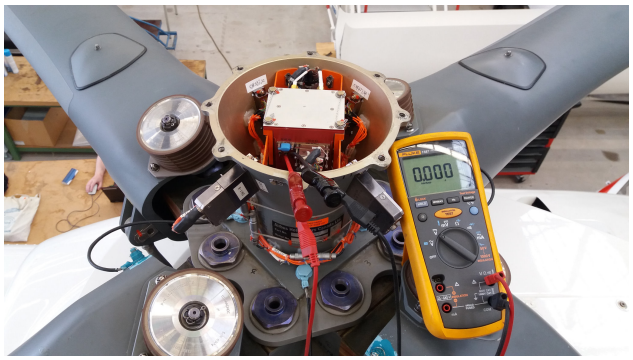

Figure 2: Sensor signal processor system of ACT/FHS's rotor measurement system

2.2. Flight Test Data

Dedicated flight tests with the ACT/FHS equipped with the rotor measurement system for system identification and model validation were conducted in summer 2019. These flight tests consist of at least three manually flown frequency sweeps with increasing frequency up to about 2 Hz for each control input at 60 knots forward flight. During the frequency sweeps, a flight state near the reference trim condition was maintained by applying uncorrelated, pulse-type inputs to the secondary controls only. In this way, cross-correlation between the four control inputs are minimized. In addition, manual 3211-multistep and step input maneuvers have been recorded at the same flight condition for model validation purposes.

For the studies of this paper, eight frequency sweeps at 60 knots have been selected from the system identification maneuvers and eight 3211-multistep maneuvers have been chosen for model validation. Additional flight tests covering standard procedures in the whole envelope and flight in turbulent air conditions (also used for turbulence modeling in [15]) are used for observer tuning and validation.

2.3. Flight Path Reconstruction and Data Pre-Processing

A post-flight flight path reconstruction consisting of two unscented Kalman filters estimates the rotatory and translatory states of the rotorcraft's center of gravity w.r.t. the local wind from raw sensor data. Both unscented Kalman filters and the used sensors are described in detail in [16]. Subsequently, the estimated states are smoothed without additional phase delay by two separate unscented Rauch-Tung-Striebel smoothers as described in [17].

Additional measurement data like the helicopter controls and rotor mast bending moments are not included in the flight path reconstruction, but are provided with a synchronized sampling time. The main rotor mast bending moments in the rotating frame, m_x and m_y, are transformed into the non-rotating frame using the rotor azimuth ψ

$$m_c = m_y \cdot \cos(\psi) + m_x \cdot \cos\left(\psi + \frac{\pi}{2}\right) \tag{1a}$$

$$m_s = m_y \cdot \sin(\psi) + m_x \cdot \sin\left(\psi + \frac{\pi}{2}\right) \tag{1b}$$

which yields the corresponding rotor mast moments m_c around the rotorcraft's pitch axis and m_s around the roll axis. Since the maximum frequency of interest is about 35 rad/s, all data is down-sampled to 40 ms which provides a Nyquist frequency twice as high. The reduced sampling time is beneficial to lower the computational costs for system identification and observer design. The rotor mast moments m_c and m_s are low-pass-filtered to suppress the 1/rev harmonic in the signals.

3. SYSTEM IDENTIFICATION

Two established system identification methods, namely the Maximum Likelihood (ML) output error method in the frequency domain and the optimized predictor-based subspace identification method (PBSIDopt) are applied to identify models from the processed flight test data. The desired models for the observer design are linear discrete-time state-space models with inputs $\boldsymbol{u}_k \in \mathbb{R}^{n_u}$, outputs $\boldsymbol{y}_k \in \mathbb{R}^{n_y}$, and states $\boldsymbol{x}_k \in \mathbb{R}^{n_x}$ of form

$$\begin{aligned} \boldsymbol{x}_{k+1} &= \boldsymbol{A}\boldsymbol{x}_k + \boldsymbol{B}\boldsymbol{u}_k \\ \boldsymbol{y}_k &= \boldsymbol{C}\boldsymbol{x}_k + \boldsymbol{D}\boldsymbol{u}_k \end{aligned} \tag{2}$$

and the number of inputs n_u, outputs n_y, and states, i.e. model order n_x. A finite number of data points $k = 1 \ldots N$ is available.

A comparison of the used system identification methods is found in [18], the next subsections give a brief description of both methods and the identified models.

3.1. Physics-based model identification

To be able to model the rotor mast bending moments m_c and m_s, an identification model structure is needed that accounts for the coupled fuselage/rotor flapping dynamics as described in Ch. 15 of [19]. Such a model consists of the 6-DoF equations of the rigid body enhanced by two first order equations for the longitudinal and lateral flapping angles β_{1c} and β_{1s} describing the motion of the tip-path plane of the rotor.

The input variables of such a model are the four pilot controls. The state vector consists of the airspeed components u, v, w, the angular rates p, q, r, the attitude angles ϕ, θ, and the flapping angles. The output vector consists of the rigid-body states, the linear accelerations a_x, a_y, a_z, the angular accelerations $\dot{p}$, $\dot{q}$, $\dot{q}$, and the rotor

mast moments.

$$
\begin{aligned}
\boldsymbol{u} &= \begin{pmatrix} \delta_x & \delta_y & \delta_p & \delta_0 \end{pmatrix}^T \\
\boldsymbol{x} &= \begin{pmatrix} u & v & w & p & q & r & \phi & \theta & \beta_{1c} & \beta_{1s} \end{pmatrix}^T \\
\boldsymbol{y} &= \begin{pmatrix} u & v & w & p & q & r & \phi & \theta & a_x & a_y & a_z \\ & & & \dot{p} & \dot{q} & \dot{r} & m_c & m_s \end{pmatrix}^T
\end{aligned} \tag{3}
$$

The mast moments are directly proportional to the flapping angles for physical reasons and thus can be used instead of the flap angle measurements. This proportionality has been illustrated in [20] with measurements from the Bo 105 helicopter.

$$
\begin{aligned}
m_c &= f_c \beta_{1c} \\
m_s &= f_s \beta_{1s}
\end{aligned} \tag{4}
$$

In the standard formulation from [19], the rotor equations consider the flapping response to angular shaft motion only, whereas the flapping response to translation and the resulting rotor contributions to the forces and moments on the fuselage are contained in the quasi-steady speed derivatives.

Using mast moments as output variables showed that also the flapping response to collective control and to translation has to be incorporated in the flapping angle equations to be able to correctly match the mast moments with equation (4). Thus the standard formulation was modified so that

- the quasi-steady cross-axis collective control derivatives X_{δ_0}, Y_{δ_0}, L_{δ_0}, M_{δ_0} were replaced by the corresponding control derivatives Lf_{δ_0} and Mf_{δ_0} in the flapping equations and
- the derivatives Lf_v, Lf_w, Mf_v and Mf_w were introduced to model the flapping response to translation.

The final equations after a model reduction to remove insignificant derivatives are

$$
\begin{aligned}
\dot{u} &= X_u u + X_w w - w_0 q + (X_r + v_0) r + g\beta_{1c} \\
&\quad + X_{\delta_x}\delta_x + X_{\delta_y}\delta_y + X_{\delta_p}\delta_p - g\cos\theta_0\theta \\
\dot{v} &= Y_v v + w_0 p - u_0 r - g\beta_{1s} + Y_{\delta_p}\delta_p \\
&\quad + g\cos\phi_0\cos\theta_0\phi - g\sin\phi_0\sin\theta_0\theta \\
\dot{w} &= Z_u u + Z_w w + (Z_p - v_0) p + u_0 q + Z_{\delta_x}\delta_x \\
&\quad + Z_{\delta_0}\delta_0 - g\sin\phi_0\cos\theta_0\phi - g\cos\phi_0\sin\theta_0\theta \\
\dot{p} &= L_r r + L_{\beta_{1s}}\beta_{1s} \\
\dot{q} &= M_r r + M_{\beta_{1c}}\beta_{1c} + M_{\delta_p}\delta_p \\
\dot{r} &= N_u u + N_v v + N_p p + N_q q + N_r r + N_{\delta_x}\delta_x \\
&\quad + N_{\delta_y}\delta_y + N_{\delta_0}\delta_0 + N_{\delta_p}\delta_p \\
\dot{\phi} &= p + \sin\phi_0\tan\theta_0 q + \cos\phi_0\tan\theta_0 r \\
\dot{\theta} &= \cos\phi_0 q - \sin\phi_0 r
\end{aligned} \tag{5}
$$

for the rigid body and

$$
\begin{aligned}
\tau_f\dot{\beta}_{1c} &= -\beta_{1c} + Mf_{\beta_{1s}}\beta_{1s} + \tau_f q + Mf_v v \\
&\quad + Mf_{\delta_x}\delta_x + Mf_{\delta_y}\delta_y + Mf_{\delta_0}\delta_0 \\
\tau_f\dot{\beta}_{1s} &= -\beta_{1s} + Lf_{\beta_{1c}}\beta_{1c} + \tau_f p + Lf_v v + Lf_w w \\
&\quad + Lf_{\delta_x}\delta_x + Lf_{\delta_y}\delta_y + Lf_{\delta_0}\delta_0
\end{aligned} \tag{6}
$$

for the flapping angles where τ_f denotes the flapping time constant. Time delays are estimated for all control inputs.

The ML frequency domain system identification is performed using a frequency range of 0.5-15 rad/s. The identification with the ML method yields continuous state-space models. As the derivation of the rotor-state observer needs discrete-time models, the identified models are converted into discrete form using a zero-order hold transformation.

3.2. Predictor-Based Subspace Identification

In contrast to physics-based model identification approaches, the PBSIDopt method yields black-box state space models, i.e. the resulting models have fully populated system matrices and non-physical states. Nonetheless, the PBSIDopt method has been successfully applied to ACT/FHS data and has shown very good model performance and applicability, see [21–25].

The following steps are performed within the PBSIDopt procedure:

1. A high-order vector-ARX model (AutoRegressive model with eXogenous input) is estimated solving a regularized linear least-squares problem.
2. The discrete model states are reconstructed from the ARX parameters and a singular value decomposition.
3. The discrete-time state-space matrices are estimated in a least-squares sense comprising the measured inputs, outputs and reconstructed states.

The PBSIDopt method was introduced and described in [26–28].

Analog to the physics-based model identification, the input vector for the PBSIDopt models consists of the four pilot controls. The airspeed components, the angular rates, the two attitude angles, and the rotor mast moments are chosen as model outputs

$$
\begin{aligned}
\boldsymbol{u}_k &= \begin{pmatrix} \delta_x & \delta_y & \delta_p & \delta_0 \end{pmatrix}^T \\
\boldsymbol{y}_k &= \begin{pmatrix} u & v & w & p & q & r & \phi & \theta & m_c & m_s \end{pmatrix}^T .
\end{aligned} \tag{7}
$$

The PBSIDopt method does not require initial model parameters or a model structure, but three integer parameter $\mathtt{p}$ (past window length), $\mathtt{f}$ (future window length) and n_x (the model order) have to be chosen. For this paper, nearly 18 000 models are identified varying the three parameters in an automatic procedure. Four different models with the model order n_x of 8, 10, 12 and 14 are then

selected from these models using the selection criterion described in [24]. Basically, the best models w.r.t. the overall index of agreement $\underline{d}_1$ (for details, see the next subsection) are considered, if they satisfy a specific assumption of the PBSIDopt method.

In figure 3, the distribution of the overall index of agreement $\underline{d}_1$ of the mast moments is shown as function of the model order n_x. The median of $\underline{d}_1$ is depicted as a black solid line, whereas the minimum and maximum are indicated as black dots. The area between the first and third quartile (Q_1 and Q_3) is given in shaded gray. The $\underline{d}_1$ of the selected models are marked with crosses. It can be seen, that the models with nearly the highest $\underline{d}_1$ are chosen for further analysis.

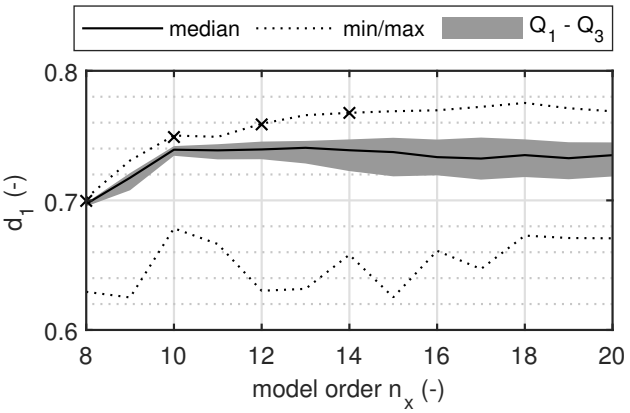

Figure 3: Distribution of overall index of agreement $\underline{d}_1$ for all models w.r.t. to the model order n_x

In addition to the full models described in equation (7), reduced "cyclic" models are identified. These models use the two cyclic controls as inputs and the roll and pitch rates as well as the rotor mast moments m_c and m_s as outputs only:

$$\begin{aligned} \boldsymbol{u}_{k,cyclic} &= \begin{pmatrix} \delta_x & \delta_y \end{pmatrix}^T \\ \boldsymbol{y}_{k,cyclic} &= \begin{pmatrix} p & q & m_c & m_s \end{pmatrix}^T . \end{aligned} \tag{8}$$

Thus, the "cyclic" models cover the main axes of the rotor mast moments and neglect the off-axes completely. In consequence, only a subset of the flight test data (only those with cyclic control excitation) are used to identify and validate these models. For further analysis, two "cyclic" models are selected with model order n_x of 8 and 10.

3.3. Model Comparison

All models are compared applying performance measures both in the time and frequency domain. In the time domain, the models are compared using eight manual 3211-multistep maneuvers. For each model and maneuver an output offset $\boldsymbol{y}_0$ and initial model states $\boldsymbol{x}_0$ are estimated to minimize the output error. This procedure is limited to the eight most significant model states to avoid favoring high-order models. The algorithm used for estimating $\boldsymbol{y}_0$ and $\boldsymbol{x}_0$ is described in detail in [24].

The most common performance measure for rotorcraft models validated in time domain is the root mean squared fit error J_{rms}

$$J_{\mathrm{rms}} = \sqrt{\frac{1}{N \cdot n_y} \sum_{k=1}^{N} \left(\boldsymbol{y}_{\mathrm{m},k} - \boldsymbol{y}_k\right)^T \left(\boldsymbol{y}_{\mathrm{m},k} - \boldsymbol{y}_k\right)} \tag{9}$$

between the measurements $\boldsymbol{y}_{\mathrm{m},k}$ and the simulation outputs $\boldsymbol{y}_k$. As proposed in Ch. 14 of [19], the velocities are scaled to ft/s while angular rates and attitudes are transformed to deg/s and deg respectively.

In addition, the index of agreement d_1 is used as a dimensionless performance criterion, see [29]. The index of agreement is normalized between 0 and 1 and, since it is dimensionless, it is neither affected by output scaling (i.e. physical units) nor the perturbation magnitude. Thus, the index of agreement is an excellent measure to compare different model outputs with diverse units. The index of agreement d_1 of one output is defined as

$$d_1 = 1 - \frac{\sum_{k=1}^{N} |y_{\mathrm{m},k} - y_k|}{\sum_{k=1}^{N} \left(|y_{\mathrm{m},k} - \overline{y}_{\mathrm{m}}| + |y_k - \overline{y}_{\mathrm{m}}|\right)} \tag{10}$$

with the mean of the corresponding measurement $\overline{y}_{\mathrm{m}}$. $d_1 = 1$ indicates a perfect match. The overall index of agreement comprising several outputs is calculated by their geometric mean respectively

$$\underline{d}_1 = \prod_{i=1}^{n_y} \left(d_{1,i}\right)^{\frac{1}{n_y}} . \tag{11}$$

Remark: The geometric mean is multiplicative and the overall index of agreement $\underline{d}_1$ becomes zero, if only one $d_{1,i}$ is zero, i.e. one model output has poor performance.

Additionally, the coherence-weighted frequency domain cost function J_{f} as used in CIFER® and described in Ch. 11 of [19] is used. In this paper, the cost functions $J_{\mathrm{f},i}$ are evaluated for a frequency range of 0.3-20 rad/s. The overall cost function J_{ave} is given as the average of n_{TF} individual frequency domain cost functions

$$J_{\mathrm{ave}} = \frac{1}{n_{\mathrm{TF}}} \sum_{i=1}^{n_{\mathrm{TF}}} J_{\mathrm{f},i} . \tag{12}$$

J_{ave} is well suited to evaluate the model accuracy in the frequency domain.

In table 1, the described model performance measures are specified for the identified models. In the first columns, the number of inputs n_u, output n_y, and states n_x are given. Please note, that the "cyclic" models only contain a subset of model inputs and outputs. Therefore, the corresponding model metrics are not directly comparable to the other model's. The model performance

Table 1: Performance measures of identified models

model name	n_u	n_y	n_x	$J_{\text{rms,RB}}$	$J_{\text{rms,MM}}$	$d_{1,\text{RB}}$	$d_{1,\text{MM}}$	$J_{\text{ave,RB}}$	$J_{\text{ave,MM}}$
n8cycl	2	4	8	2.32	301.2	0.876	0.733	195.9	247.1
n10cycl	2	4	10	2.25	233.4	0.884	0.762	86.1	85.5
n8full	4	10	8	2.46	202.3	0.817	0.699	242.4	467.8
n10full	4	10	10	2.45	174.1	0.825	0.748	191.0	90.3
n12full	4	10	12	2.55	169.5	0.827	0.757	194.2	71.1
n14full	4	10	14	1.98	166.9	0.845	0.766	219.8	77.0
n10phy	4	10	10	2.02	254.6	0.829	0.644	134.2	388.1

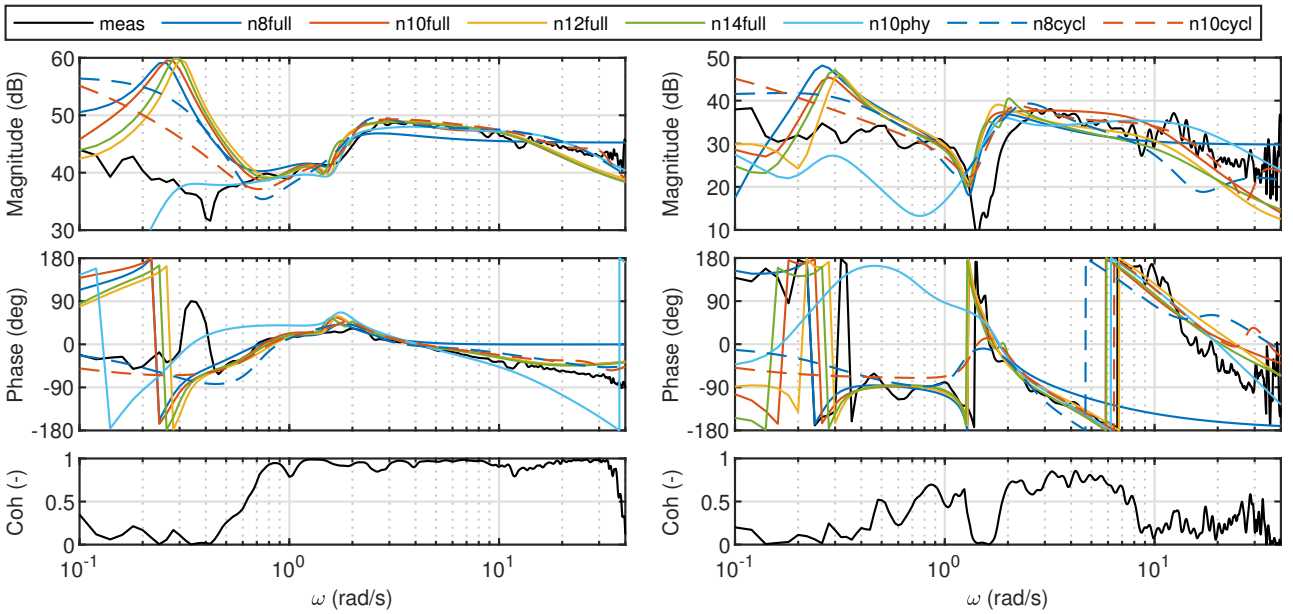

(a) longitudinal cyclic δ_x to m_c (on-axis)

(b) longitudinal cyclic δ_x to m_s (off-axis)

Figure 4: Transfer functions of identified models in comparison to measured frequency response

measures are separated into a rigid-body measure (index $_{\text{RB}}$ with the units described before) and a rotor mast moment measure (index $_{\text{MM}}$, evaluated in Nm).

The best time domain performance measures are observed using the n14full model. Since the used PBSIDopt method works in the time domain, this result is not surprising. Nonetheless, the differences regarding the time-domain measures are small, especially looking at the rigid-body outputs only ($J_{\text{rms,RB}}$ and $d_{1,\text{RB}}$). The physical model n10phy shows a very good rigid-body output rms error $J_{\text{rms,RB}}$, but is outperformed by the rotor mast moment measure of the other (full) models.

The models n10full, n12full and n14full result in very similar frequency domain costs J_{ave}. Nonetheless, n12full is slightly better than n14full. The physical model n10phy shows similar results as in the time domain: the rigid-body outputs are accurately modeled, but the rotor mast moments still show deficits. Since the physical model n10phy covers additional rigid body outputs compared to the black-box PBSIDopt models, this is not surprisingly. Furthermore, n10phy only offers 39 free parameters based on the chosen model structure, whereas the PBSIDopt model n10full has 158 free parameters.

In figure 4 the on-axis responses of all models from longitudinal cyclic input to m_c (pitch) and the corresponding off-axis responses from δ_x to m_s (roll) are shown. The measured frequency response generated from sweep data is shown in black ("meas"). All models, except for n8full, match the on-axis frequency response in the frequency range of 1-10 rad/s precisely. The off-axis response is captured accurately by all models, except n8full and n10phy.

In summary, all identified models have pros and cons regarding the different performance measures. From the values given in table 1, it would be difficult to choose the most appropriate model for observer design. So, all models are used in the next section to design an observer for rotor mast moment estimation and based on the corresponding observer performance the final observer model is chosen.

4. OBSERVER DESIGN

The goal of this paper is to design an observer that accurately estimates the rotor mast moments m_c and m_s based on measurements of the pilot controls and the rigid-body states only. The observer design process is separated into three steps.

1. A steady-state Kalman filter forms the core of the design. It provides a simple yet tunable parametrization of the observer gain that is guaranteed to yield stable observer dynamics.
2. The second step is the data-driven optimization. Classical Kalman filter design offers the opportunity to account for knowledge about model deficiencies. However, it is usually difficult to determine and quantify those inaccuracies. This is especially true in the case of non-physical process models. The observer gain is hence tuned using flight test data directly.
3. In order to investigate which observer configuration is expected to achieve the best performance, a cross-validation procedure is conducted on a carefully compiled data set covering the most commonly encountered flight conditions.

The next subsections elucidates the observer structure including the optimization parameters, data selection and the cross-validation process to select the designed observer.

4.1. Observer Structure

An observer is essentially a copy of the system augmented by a correction term that adapts the state predictions in case of errors between measured and predicted quantities. This error enters into the state equations by multiplication with the observer gain matrix $\boldsymbol{L}$. A convenient way to design this gain is to apply Kalman filter theory. Typically, it is assumed that the state equations are disturbed by a zero-mean white process noise $\boldsymbol{w}_k$ with covariance matrix $\boldsymbol{W}$ and that the output equation is disturbed by a zero-mean white measurement noise $\boldsymbol{v}_k$ with covariance matrix $\boldsymbol{V}$. However, for the remainder of this paper, these matrices are considered merely as tuning parameters rather than covariance matrices related to a stochastic process describing potential model deficiencies.

The observer design model reads as follows

$$\begin{aligned} \boldsymbol{x}_{k+1} &= \boldsymbol{A}\boldsymbol{x}_k + \boldsymbol{B}\boldsymbol{u}_k + \boldsymbol{w}_k \\ \boldsymbol{y}_{\mathrm{o},k} &= \boldsymbol{C}_1\boldsymbol{x}_k + \boldsymbol{D}_1\boldsymbol{u}_k + \boldsymbol{v}_k \\ \boldsymbol{z}_k &= \boldsymbol{C}_2\boldsymbol{x}_k + \boldsymbol{D}_2\boldsymbol{u}_k, \end{aligned} \tag{13}$$

where

$$\begin{aligned} \boldsymbol{u}_k &= \begin{pmatrix} \delta_x & \delta_y & \delta_p & \delta_0 \end{pmatrix}^T \\ \boldsymbol{y}_{\mathrm{o},k} &= \begin{pmatrix} w & p & q & r & \phi & \theta \end{pmatrix}^T \end{aligned} \tag{14}$$

for the physics-based and the regular (full) PBSIDopt models. Only the following subset of inputs and outputs are used for the reduced "cyclic" PBSIDopt models

$$\begin{aligned} \boldsymbol{u}_k &= \begin{pmatrix} \delta_x & \delta_y \end{pmatrix}^T \\ \boldsymbol{y}_{\mathrm{o},k} &= \begin{pmatrix} p & q \end{pmatrix}^T. \end{aligned} \tag{15}$$

The performance output vector (which is estimated) is formed by the rotor mast moments

$$\boldsymbol{z}_k = \begin{pmatrix} m_c & m_s \end{pmatrix}^T. \tag{16}$$

$\boldsymbol{C}_1, \boldsymbol{C}_2, \boldsymbol{D}_1, \boldsymbol{D}_2$ are defined by the corresponding rows of $\boldsymbol{C}$ and $\boldsymbol{D}$, respectively. The longitudinal and lateral velocity components u and v are omitted from the estimation, since the data only consists of forward flight maneuvers at 60 knots. For all models considered, $(\boldsymbol{A}, \boldsymbol{C}_1)$ is observable. In summary, only control inputs and the measured outputs $\boldsymbol{y}_{\mathrm{o},k}$ are used to estimate the selected performance outputs $\boldsymbol{z}_k$.

The Kalman filter equations consist of two parts, a correction and a prediction step. First, the state estimate from the previous step $\hat{\boldsymbol{x}}_{k|k-1}$ is updated (corrected) by adding the weighted estimation error

$$\hat{\boldsymbol{x}}_{k|k} = \hat{\boldsymbol{x}}_{k|k-1} + \boldsymbol{L}\left(\boldsymbol{y}_{\mathrm{o},k} - \boldsymbol{C}_1\hat{\boldsymbol{x}}_{k|k-1} - \boldsymbol{D}_1\boldsymbol{u}_k\right). \tag{17}$$

The updated state $\hat{\boldsymbol{x}}_{k|k}$ is then used to predict the system dynamics one step ahead in time

$$\begin{aligned} \hat{\boldsymbol{x}}_{k+1|k} &= \boldsymbol{A}\hat{\boldsymbol{x}}_{k|k} + \boldsymbol{B}\boldsymbol{u}_k, \quad \hat{\boldsymbol{x}}_0 = \boldsymbol{0} \\ \hat{\boldsymbol{y}}_{\mathrm{o},k|k} &= \boldsymbol{C}_1\hat{\boldsymbol{x}}_{k|k} + \boldsymbol{D}_1\boldsymbol{u}_k \\ \hat{\boldsymbol{z}}_{k|k} &= \boldsymbol{C}_2\hat{\boldsymbol{x}}_{k|k} + \boldsymbol{D}_2\boldsymbol{u}_k. \end{aligned} \tag{18}$$

By design, the observer gain $\boldsymbol{L}$ is given by

$$\boldsymbol{L} = \boldsymbol{P}\boldsymbol{C}_1^T\left(\boldsymbol{C}_1\boldsymbol{P}\boldsymbol{C}_1^T + \boldsymbol{V}\right)^{-1}, \tag{19}$$

where the matrix $\boldsymbol{P}$ is positive definite and the solution to the discrete-time algebraic Riccati equation

$$\begin{aligned} \boldsymbol{P} = \boldsymbol{A}\boldsymbol{P}\boldsymbol{A}^T - \boldsymbol{A}\boldsymbol{P}\boldsymbol{C}_1^T\left(\boldsymbol{C}_1\boldsymbol{P}\boldsymbol{C}_1^T + \boldsymbol{V}\right)^{-1}\left(\boldsymbol{A}\boldsymbol{P}\boldsymbol{C}_1^T\right)^T \\ + \boldsymbol{W}^T. \end{aligned} \tag{20}$$

Hence, $\boldsymbol{L}$ is parameterized by the matrices $\boldsymbol{W}$ and $\boldsymbol{V}$. If they are both positive definite, then the observer dynamics are guaranteed to be stable [30]. Hence, to ensure stability, $\boldsymbol{W}$ is assumed to be given as $\boldsymbol{W} = \boldsymbol{S}\boldsymbol{S}^T$ with an invertible, triangular matrix $\boldsymbol{S}$ and $\boldsymbol{V}$ is assumed to be diagonal with positive entries.

The benefit of this approach is, that the observer performance can be optimized in a straight-forward manner based on recorded reference data. To that end, the quadratic cost function

$$f(\boldsymbol{W}, \boldsymbol{V}) := \sum_{k=0}^{N} \|\boldsymbol{z}_k - \hat{\boldsymbol{z}}_{k|k}\|^2 \tag{21}$$

is introduced. It measures the error between recorded and estimated rotor mast moments for a given flight test

of $N+1$ samples and for each pair of (positive definite) tuning matrices $(\boldsymbol{W}, \boldsymbol{V})$. This is a sum-of-squares problem, that can be efficiently solved by a gradient-based solver (e.g. MATLAB's `lsqnonlin`) when combined with a multi-start strategy [31]. The optimization variables are the entries of $\boldsymbol{W}$ and $\boldsymbol{V}$, respectively. In the following, two cases are distinguished:

- Case 1 assumes that $\boldsymbol{S}$ is diagonal ("diag") and thus $\boldsymbol{W}$ is also diagonal.
- Case 2 assumes that $\boldsymbol{S}$ is upper triangular ("tria") and thus $\boldsymbol{W}$ is dense (fully populated).

4.2. Data Selection and Cross-Validation

This paper focuses on forward flight conditions at 60 knots. The overall duration of the available data is about one hour. The data is partitioned into three sets, as depicted in figure 5:

- The training set T_{train} contains all data that is used when minimizing equation (21). It comprises step and 3211-multistep inputs for each axis as well as segments of calm and turbulent flights of variable length with a total duration of 15 minutes.
- The test set $T_{\text{test},1}$ contains similar maneuvers as T_{train}, but with a larger amount of routine flight data and an accumulated duration of about only 10 minutes. This set is used for discrete optimization over the initial values of the multi-start optimizer.
- The test set $T_{\text{test},2}$ contains sweep maneuvers for each axis and additional flight data in calm and turbulent atmosphere. This set is irrelevant within the observer optimization process and is used for validation purposes in section 5 only. Its total duration is about 35 minutes.

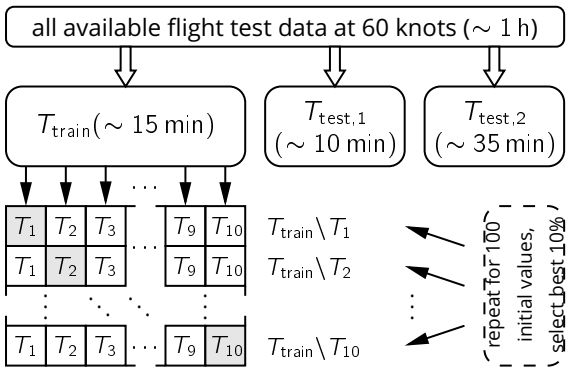

Figure 5: Flight test data partition and cross-validation scheme

Seven system models and two structural choices for $\boldsymbol{W}$ are available resulting in a total number of fourteen observer design configurations. A tenfold cross-validation is employed to determine the observer design structure with the best predictive capabilities. For that purpose, the training set T_{train} is manually partitioned into ten subsets $T_1, \ldots, T_{10}$ of 90 seconds duration each. Care was taken, that each subset contains various maneuvers exciting all axes sufficiently. The cross-validation process for each observer configuration consists of ten runs. In each run, another subset is excluded from T_{train} for the optimization of the observer gain and is instead used for validation. Each run is repeated 100 times for different initial values of $\boldsymbol{W}$ and $\boldsymbol{V}$ as a multi-start strategy. The cross-validation performance for each subset is calculated as the mean value over the best 10 repetitions. The cross-validation (cv) results are visualized in figure 6 for the observer designs under scrutiny. For each identified model, the cv errors of each run, the respective means and 95 % confidence intervals (ci) are depicted for both structures of $\boldsymbol{W}$ ("diag" and "tria") side by side.

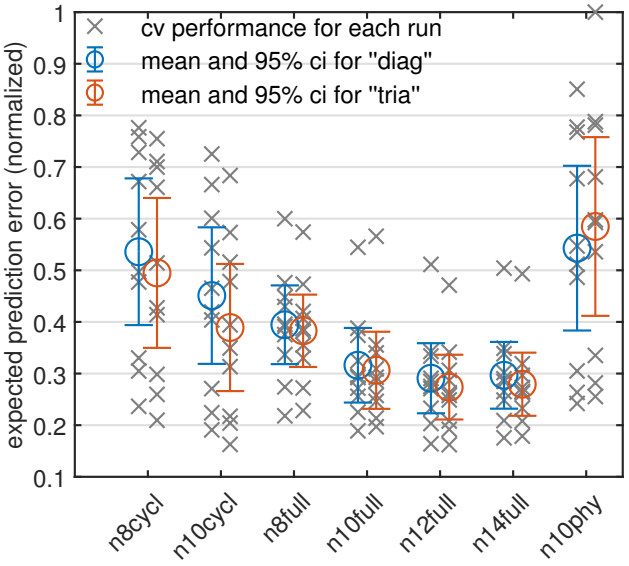

Figure 6: Cross-validation results for different observer design configurations

In general, the results follow a similar trend as the model validation measures $J_{\text{rms,MM}}$ and $d_{1,\text{MM}}$ in section 3.3. This is comprehensible, since the observer estimation error from equation (21) is comparable to $J_{\text{rms,MM}}$ albeit the observers are evaluated on a much larger data set. At the same time, the rigid-body error measures do not seem to have a major impact on the expectable observer performance. The best observer performance can be expected from the higher-order PBSIDopt models n10full, n12full and n14full since they attain not only the lowest error mean values but also exhibit the least variance in their estimates meaning that they are supposed to deliver their average performance more consistently. Somewhat surprising is the fact that even the reduced "cyclic" models outperform the physics-based model n10phy. This fact and the low model performance regarding the rotor mast moments indicates that the model structure imposed by physical modeling could be too restrictive and might not be able to capture rotor states as well as the off-axis responses well enough.

In conclusion, the impact of different structures of $\boldsymbol{W}$ is rather minor. More tuning parameters usually yield

(slightly) improved prediction results. However, especially for the full PBSIDopt models the benefits are only marginal. This might be due to the fact that those models already perform quite well and, hence, the observer already acts quite optimal when tuned with a diagonal W. Another reason could be that it is less likely to find a good local optimum for the observer when having such many tuning parameters.

According to figure 6, no additional benefit can be seen in increasing the model complexity beyond 12 states as the mean and ci for n14full become slightly worse. Therefore, for the following investigations, the model n12full is selected for the observer design together with a dense, positive definite W ("tria"). This observer configuration is optimized on the complete set T_{train} for 1 000 different initial values of W and V. The resulting observers are then validated on $T_{\text{test},1}$ and the best performing one is selected. For comparison purposes, the cyclic model n10cycl with dense W is optimized in the same way.

5. RESULTS

5.1. Time Domain Evaluation

Figure 7a shows the measured and estimated rotor mast moments for a section of forward flight in moderate turbulence rated with level 6 using the Turbulent Air Scale [32] ("Medium bumps with occasional heavy ones"). In general, the performance of both observers is very good despite turbulent excitation of the rotorcraft. The estimated rotor mast moments do not suffer from noteworthy time delays and the short-term behavior seems adequate. In detail, both observers exhibit comparable lateral mast moment (m_s) estimates, while the less complex n10cycl model performs slightly better for the longitudinal axis (m_c) from second four onwards. This can be confirmed by computing the prediction error in equation (21) which is about 22% lower for the n10cycl observer. Thus, there are examples, especially flights with negligible collective inputs, where the reduced observer n10cycl performs better although the n12full observer has a better average performance.

The measured and estimated mast moments during a coordinated turn are compared in figure 7b. The measured rotor mast moments are accurately reproduced during the first 20 seconds of the run. Then, the estimated longitudinal mast moments m_c slowly diverge from the measurements when the rotorcraft starts to turn. During the turn, headwind becomes crosswind which is then compensated by roll angle and lateral cyclic as well as pedal inputs. In an analogous manner, forward (air-) speed is reduced, longitudinal cyclic input and pitch angle are adjusted. Hence, this maneuver violates the near-trim assumption and therefore cannot be covered by the observer unless changing trim conditions are accounted for in its design. Still, the mid- and high-frequency components of the estimated rotor mast moments match the measurements. The frequency domain evaluation in the next subsection gives more details.

5.2. Frequency Domain Evaluation

The plots in figure 8 show frequency responses from the measured rotor mast moments z_i to the corresponding observations $\hat{z}_i$ for $i = 1 \ldots 2$, which is also known as the error response function

$$\epsilon_i(\omega) = \frac{\hat{z}_i(\omega)}{z_i(\omega)}, \; i = 1 \ldots 2. \tag{22}$$

The error response functions $\epsilon_i(\omega)$ are calculated for all data in the set $T_{\text{test},2}$. Every run has a duration of 100 to 120 seconds. The total duration is about 35 minutes. The different colors visualize on-axis maneuvers (i.e. pitch or roll axis sweeps respectively), collective sweep maneuvers and all remaining maneuvers (i.e. calm forward flight, turbulent flight and pedal sweeps).

An error response function with 0 dB magnitude and 0 deg phase implies an ideal match between measurement and estimation and thus, a perfect observer. For illustration purposes, the phase plots of a 10 ms, 25 ms and 50 ms time delay are shown.

Since frequency responses are only meaningful where the coherence is high enough, the color of the error response plots fades out when the coherence gets worse (i.e. the color becomes up to 50% lighter till the coherence reaches 0.55). This mainly affects the forward flight data in calm and turbulent atmosphere as well as pedal inputs which hardly excite the mast moments. Furthermore, the low frequencies are often faded out due to low coherence. In general, the other sweep data have high coherence between 0.4 and 30 rad/s indicated by fully saturated color.

In all cases, the estimated on-axis responses match the reference data accurately over a large frequency range from 1 to 30 rad/s. Nonetheless, the low-frequency responses suffer from trim deviation as described before or are faded out, since coherence is low. The most apparent difference between both observers is their performance w.r.t. collective sweeps. Here, the reduced n10cycl observer mostly underestimates the magnitude, whereas the n12full observer nearly reaches on-axis performance. Therefore, the inclusion of the collective input in the n12full model clearly pays off and leads to much smaller estimation errors, especially in the pitch axis. Regarding the other flight data, both observers tend to underestimate rather than overestimate the signal magnitudes for mid and high frequencies. In most cases, the 2 dB magnitude (about 25% overshoot) line is not exceeded, but up to 40% underestimation (about -4 dB) can be observed for frequencies between 1 and 20 rad/s.

The phase delay of both observers is less than 10 ms for the on-axis sweep data. Collective sweep data pro-

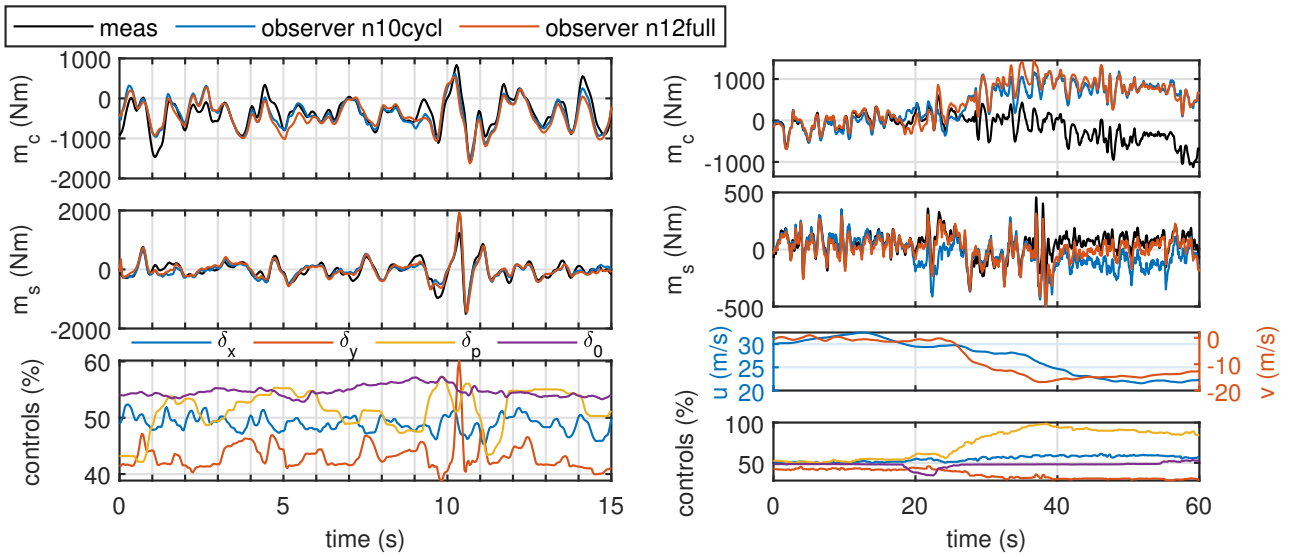

(a) Turbulence flight level 6, [32]

(b) Coordinated turn with head- and crosswind

Figure 7: Time domain comparison of measured and estimated rotor mast moments

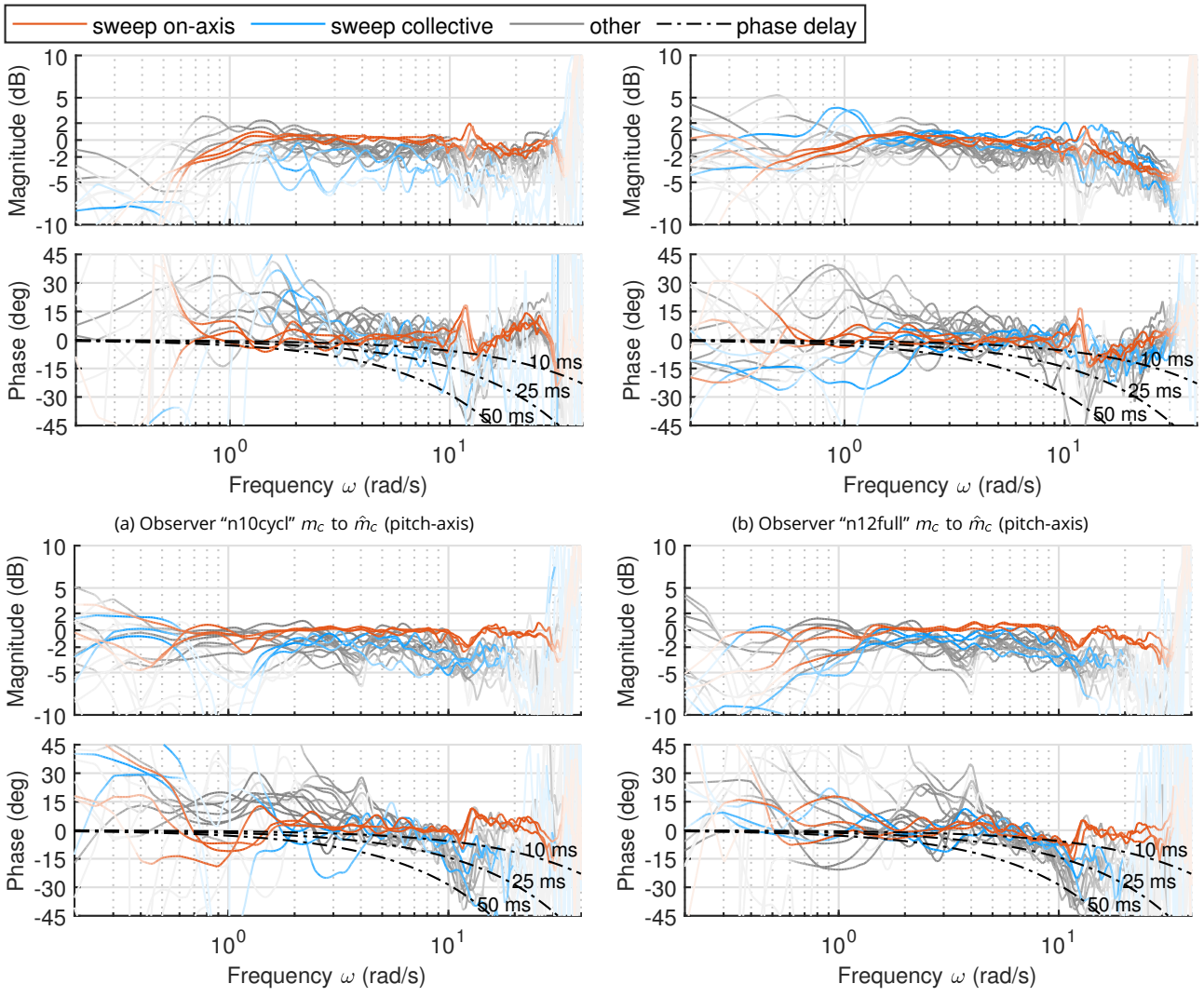

(a) Observer "n10cycl" m_c to $\hat{m}_c$ (pitch-axis)

(b) Observer "n12full" m_c to $\hat{m}_c$ (pitch-axis)

(c) Observer "n10cycl" m_s to $\hat{m}_s$ (roll-axis)

(d) Observer "n12full" m_s to $\hat{m}_s$ (roll-axis)

Figure 8: Error response functions $\epsilon(\omega)$ from measured rotor mast moment z to estimation $\hat{z}$

cessed by the full observer n12full only shows a small difference to the on-axis behavior between 1 and 14 rad/s. At larger frequencies, a phase delay of up to 25 ms can be observed. Some of the other flight test data suffer from larger phase delays up to 50 ms, especially for turbulent flight conditions. In general, the longitudinal mast moment has a smaller phase delay than the lateral mast moment.

6. CONCLUSIONS AND FUTURE WORK

Observers can be a cost-effective alternative for non-standard sensors like rotor measurement devices. This paper demonstrates how the observer tuning problem can be approached in practice such that the designed observer captures the sensor behavior suitably well. To that end, various system models have been identified and evaluated w.r.t. their expected observer performance using a cross-validation procedure. The tuning process itself is carried out by direct optimization of recorded reference flight test data and thus ensures good predictions under real flight conditions.

The following conclusions are drawn from this work:

1. The main rotor mast moment dynamics can already be captured by reduced "cyclic" black-box models.
2. More complex rotorcraft models yield improved results regarding maneuvers with significant collective inputs.
3. A good system model is key to peak observer performance. Balancing the rigid-body and the rotor mast moment model performance is essential.
4. The rotor mast moment prediction errors of the applied system models seem to be a good indicator for the expectable observer performance. The better system models used for observer design perform (in terms of model validation measures), more degrees of freedom for observer tuning do not yield performance benefits.
5. Optimization-based tuning allows to adapt observer performance also for non-physical black-box models which are hard to tune manually.
6. Data-driven observer tuning is an effective way to adapt the observer estimates to reference data.
7. The tuned observers also exhibit good frequency response characteristics although not specifically accounted for during optimization.
8. The observer phase delay is less then 10 ms for on-axis sweeps, but can reach up to 50 ms for high frequencies regarding other flight test data.

Future work will cover the application of the designed observers. Furthermore, the presented observer design approach needs to be extended to the full flight envelope. It is clear that the presented approach can be applied without modification to any other forward flight velocity as long as appropriate models and suitable flight test data are available. The challenge will be to predict the offset/trim value changes occurring during dynamic maneuvers such as acceleration and deceleration as well as changing wind conditions. A possible concept might include an additional low-frequency observer based on trim curve information enhancing the presented mid-frequency observer by reasonable offset or trim value estimates.

Author contact:
Johannes Wartmann: johannes.wartmann@dlr.de
Frederik A. Döring: frederik.doering@dlr.de
Susanne Seher-Weiß: susanne.seher-weiss@dlr.de

ACKNOWLEDGMENT

The investigations were conducted under the auspices of the national research project CORINNE (Comfort of Ride Improved Engineering) funded by the German Federal Ministry for Economic Affairs and Energy within the German Aviation Research Program LuFo V-3.

Supported by:

Federal Ministry
for Economic Affairs
and Energy

on the basis of a decision
by the German Bundestag

The authors would like to thank everyone involved during the planning, preparation, and execution of the flight tests, in particular the flight test crew Uwe Göhmann, Sebastian Soffner, and Waldemar Krebs, as well as Klaus Alvermann and Volker Plaßmeier.

References

[1] W. E. Hall Jr. and A. E. Bryson Jr. Inclusion of Rotor Dynamics in Controller Design for Helicopters. *Journal of Aircraft*, 10(4):200–206, April 1973.

[2] Stanley J. Briczinski and Dean E. Cooper. Flight Investigation of Rotor/Vehicle State Feedback. NASA Contractor Report CR-132546, NASA, Stratford, Connecticut, USA, 1975.

[3] Marc D. Takahashi. Rotor-State Feedback in the Design of Flight Control Laws for a Hovering Helicopter. *Journal of the American Helicopter Society*, 39(1):50–62, January 1994.

[4] Joseph F. Horn, Wei Guo, and Gurbuz Taha Ozdemir. Use of Rotor State Feedback to Improve Closed-

Loop Stability and Handling Qualities. *Journal of the American Helicopter Society*, 57, 2012.

[5] Christina M. Ivler. Development and Comparison of Explicit and Implicit Rotor-State Feedback Control Systems for a Fly-by-Wire UH-60. In *American Helicopter Society Rotorcraft Handling Qualities Specialists' Meeting*, Huntsville, AL, USA, February 2014.

[6] Christina M. Ivler, Mohammadreza H. Mansur, MAJ Zachariah G. Morford, Kevin Kalinowski, and Marit E. Knapp. Flight Test of Explicit and Implicit Rotor-State Feedback Fly-By-Wire Control Laws. In *American Helicopter Society 72nd Annual Forum*, West Palm Beach, Florida, USA, May 2016.

[7] Joseph F. Horn and Nilesh Sahani. Detection and Avoidance of Main Rotor Hub Moment Limits on Rotorcraft. *Journal of Aircraft*, 41(2):372–379, March 2004.

[8] Nilesh A. Sahani, Joseph F. Horn, Geoffrey J. J. Jeram, and J. V. R. Prasad. Hub Moment Limit Protection Using Neural Network Prediction. *Journal of the American Helicopter Society*, 51(4), 2006.

[9] Umberto Saetti, Joseph F. Horn, Tom Berger, and Mark B. Tischler. Handling-Qualities Perspective on Rotorcraft Load Alleviation Control. *Journal of Guidance, Control, and Dynamics*, 43(10):1792–1804, October 2020.

[10] David J. Haas. Determination of Helicopter Flight Loads from Fixed System Measurements. In *AIAA 32nd Structures, Structural Dynamics, and Materials Conference*, Baltimore, MD, USA., April 1991.

[11] David Haas, Joel Milano, and Lance Flitter. Prediction of Helicopter Component Loads Using Neural Networks. In *AIAA 34th Structures, Structural Dynamics and Materials Conference*, La Jolla, CA, USA, April 1993.

[12] David J. Haas and Robin Imber. Identification of Helicopter Component Loads Using Multiple Regression. *Journal of Aircraft*, 31(4):929–935, July 1994.

[13] Marit E. Knapp, Christina M. Ivler, Marcos G. Berrios, Tom Berger, and Mark B. Tischler. Kalman Filter Estimation of Rotor-State Flapping: An Optimization-based Approach with UH-60 Flight Test Data. In *American Helicopter Society International 73rd Annual Forum & Technology Display*, Fort Worth, Texas, USA, May 2017.

[14] Marco Favale, Davide Prederi, and Alberto Angelo Trezzini. Prediction of AW609 Rotor Loads by Means of Neural Networks. In *Vertical Flight Society's 75th Annual Forum & Technology Display*, Philadelphia, PA, USA, May 2019.

[15] Susanne Seher-Weiß and Michael Jones. Control Equivalent Turbulence Input Models for Rotorcraft in Hover and Forward Flight. *Journal of Guidance, Control, and Dynamics*, pages 1–8, May 2021.

[16] Johannes Wartmann, Jens Wolfram, and Martin Gestwa. Sensor fusion and flight path reconstruction of the ACT/FHS rotorcraft. *CEAS Aeronautical Journal*, 6(4):529–539, December 2015.

[17] Simo Särkkä. Unscented Rauch-Tung-Striebel Smoother. *IEEE Transactions on Automatic Control*, 53(3), April 2008.

[18] Susanne Seher-Weiß and Johannes Wartmann. Initial investigation into the complementary use of black box and physics-based techniques in rotorcraft system identification. *CEAS Aeronautical Journal*, 11(2):501–513, June 2020.

[19] Mark B. Tischler and Robert K. Remple. *Aircraft and Rotorcraft System Identification: Engineering Methods with Flight-Test Examples*. American Institute of Aeronautics and Astronautics, Inc., Reston, Virginia, USA, second edition, 2012.

[20] Susanne Seher-Weiss and Wolfgang von Gruenhagen. Comparing Explicit and Implicit Modeling of Rotor Flapping Dynamics for the EC135. In *Deutscher Luft- Und Raumfahrtkongress*, Berlin, Germany, September 2012.

[21] Johannes Wartmann and Susanne Seher-Weiss. Application of the Predictor-Based Subspace Identification Method to Rotorcraft System Identification. In *39th European Rotorcraft Forum*, Moscow, Russia, September 2013.

[22] Johannes Wartmann. ACT/FHS System Identification including Engine Torque and Main Rotor Speed using the PBSIDopt Method. In *41st European Rotorcraft Forum*, Munich, Germany, September 2015.

[23] Johannes Wartmann. Closed-Loop Rotorcraft System Identification Using Generalized Binary Noise. In *American Helicopter Society International 73rd Annual Forum & Technology Display*, Fort Worth, Texas, USA, May 2017.

[24] Johannes Wartmann and Steffen Greiser. Identification and Selection of Rotorcraft Candidate Models to Predict Handling Qualities and Dynamic Stability. In *44th European Rotorcraft Forum*, Delft, The Netherlands, September 2018.

[25] Susanne Seher-Weiß, Steffen Greiser, Johannes Wartmann, Vincent Myrand-Lapierre, Arthur Gubbels, Joseph Ricciardi, and Kenneth Hui. Bell 412 System Identification: Comparing Methods and Tools. In *Vertical Flight Society's 75th Annual Forum & Technology Display*, page 17, Philadelphia, PA, USA, May 2019.

[26] Alessandro Chiuso. The role of vector autoregressive modeling in predictor-based subspace identification. *Automatica*, 43(6):1034–1048, June 2007.

[27] A. Chiuso. On the Relation Between CCA and Predictor-Based Subspace Identification. *IEEE Transactions on Automatic Control*, 52(10):1795–1812, October 2007.

[28] Alessandro Chiuso. On the Asymptotic Properties of Closed-Loop CCA-Type Subspace Algorithms: Equivalence Results and Role of the Future Horizon. *IEEE Transactions on Automatic Control*, 55(3):634–649, March 2010.

[29] Hideo Muroi and Shuichi Adachi. Model Validation Criteria for System Identification in Time Domain. In *17th IFAC Symposium on System Identification SYSID 1015*, Beijing, China, October 2015.

[30] Frank L. Lewis, Lihua Xie, and Dan Popa. *Optimal and Robust Estimation: With an Introduction to Stochastic Control Theory*. CRC Press, second edition, December 2017.

[31] Andreas Raue, Marcel Schilling, Julie Bachmann, Andrew Matteson, Max Schelke, Daniel Kaschek, Sabine Hug, Clemens Kreutz, Brian D. Harms, Fabian J. Theis, Ursula Klingmüller, and Jens Timmer. Lessons Learned from Quantitative Dynamical Modeling in Systems Biology. *PLoS ONE*, 8(9):e74335, September 2013.

[32] Anon. *Defence Standard 00-970, Design and Airworthiness Requirements for Service Aircraft, Part 7 - Rotorcraft, Section 9*. Ministry of Defence, Glasgow, Scotland, U.K., 2010.